

# Faraday Discussions

Accepted Manuscript



This manuscript will be presented and discussed at a forthcoming Faraday Discussion meeting. All delegates can contribute to the discussion which will be included in the final volume.

**Register now to attend!** Full details of all upcoming meetings: <http://rsc.li/fd-upcoming-meetings>



This is an *Accepted Manuscript*, which has been through the Royal Society of Chemistry peer review process and has been accepted for publication.

*Accepted Manuscripts* are published online shortly after acceptance, before technical editing, formatting and proof reading. Using this free service, authors can make their results available to the community, in citable form, before we publish the edited article. We will replace this *Accepted Manuscript* with the edited and formatted *Advance Article* as soon as it is available.

You can find more information about *Accepted Manuscripts* in the [Information for Authors](#).

Please note that technical editing may introduce minor changes to the text and/or graphics, which may alter content. The journal's standard [Terms & Conditions](#) and the [Ethical guidelines](#) still apply. In no event shall the Royal Society of Chemistry be held responsible for any errors or omissions in this *Accepted Manuscript* or any consequences arising from the use of any information it contains.

# Mie scatter corrections in single cell infrared microspectroscopy

Tatiana Konevskikh<sup>1</sup>, Rozalia Lukacs<sup>1</sup>, Reinhold Blümel<sup>2</sup>, Arkadi Ponossov<sup>1</sup>, Achim Kohler<sup>1</sup>

<sup>1</sup>Department of Mathematical Sciences and Technology (IMT), Norwegian University of Life Sciences, 1430 Ås, Norway

<sup>2</sup>Department of Physics, Wesleyan University, Middletown, Connecticut 06459-0155, USA

**Key Words:** Mie scattering, infrared microscopy, Extended Multiplicative Signal Correction (EMSC)

\*Corresponding author: Tatiana Konevskikh

Tel: +47 67 23 15 84

Fax: +47 64 96 54 01

E-mail: tatiana.konevskikh@nmbu.no

**Abbreviations:** Extend multiplicative signal correction (EMSC), Multiplicative signal correction (MSC), Fast Fourier transform (FFT), Principal Component Analysis (PCA)

21 **Abstract**

22 Strong Mie scattering signatures hamper the chemical interpretation and multivariate analysis of infrared  
23 microscopy spectra of single cells and tissues. During recent years, several numerical Mie scatter correction  
24 algorithms for the infrared spectroscopy of single cells have been published. In the paper at hand, we  
25 critically reviewed existing algorithms for corrections of Mie scattering and suggest improvements. We  
26 developed an iterative algorithm based on Extended Multiplicative Scatter Correction (EMSC), for the  
27 retrieval of pure absorbance spectra from highly distorted infrared spectra of single cells. The new algorithm  
28 uses the Van de Hulst approximation formula for the extinction efficiency employing a complex refractive  
29 index. The iterative algorithm involves the establishment of an EMSC meta-model. While existing iterative  
30 algorithms for the correction of resonant Mie scattering employ three independent parameters for  
31 establishing a meta-model, we could decrease the number of parameters from three to two independent  
32 parameters, which reduced the calculation time for the Mie scattering curves for iterative EMSC meta-model  
33 by a factor 10. Moreover, by employing the Hilbert transform for evaluating the Kramers-Kronig relations  
34 based on an FFT algorithm in Matlab, we further improved the speed of the algorithm by a factor 100. For  
35 testing the algorithm we simulate distorted apparent absorbance spectra by utilizing the exact theory for the  
36 scattering of infrared light at absorbing spheres taking into account the high numerical aperture of infrared  
37 microscopes employed for the analysis of single cells and tissues. In addition, the algorithm was applied to  
38 measured absorbance spectra of single lung cancer cells.

39 ..

## 40 Introduction

41 Since the invention of infrared microscopes in the 90s, infrared microscopy has become an attractive tool for  
42 the analysis of single cells and connective tissues in biological and medical sciences<sup>1</sup>. Via infrared  
43 microscopy, tissues and cells can be analysed chemically without destroying the chemical structure of the  
44 material. Unfortunately, strong scatter effects that hamper the chemical interpretation of spectra occur, which  
45 have been interpreted as Mie-type scattering<sup>2</sup>. According to Mie theory<sup>3, 4</sup>, single cells are highly efficient  
46 scatterers in the infrared, since the wavelength of the infrared radiation is the same order as the size of the  
47 cells.

48 The correction of Mie type scattering in infrared spectra of single cells is difficult, since scattering and  
49 absorption are highly entangled. The reason for this is that due to the strong scattering, a large part of the  
50 scattered light does not reach the detector: only scattered light that is collected by the Schwarzschild optics  
51 reaches the detector, while a substantial part of the light is scattered into solid angles, which are not covered  
52 by the Schwarzschild optics. The scattered light that does not reach the detector leads to apparent absorption  
53 signatures in the measured absorbance spectrum, and the researcher is at a loss to decide which part of the  
54 measured absorbance spectrum is due to scattering and which part is due to chemical absorption. Thus, in  
55 FTIR microspectroscopy of single cells, the measured absorbance spectrum is also termed the apparent  
56 absorbance spectrum, since it contains both absorption and scattering signatures. Due to the difficulties in the  
57 interpretation of absorption peaks, scattering and absorption of infrared radiation at cells have been studied  
58 during recent years and algorithms have been established to separate scattering and absorption in apparent  
59 absorbance spectra in infrared spectroscopy of single cells<sup>5-11</sup>. All established algorithms, are based on Mie-  
60 theory, an exact theory for the scattering of infrared light at absorbing spheres developed by Gustav Mie in  
61 1905<sup>3</sup>. The theory describes the scattering of electromagnetic radiation at spheres rigorously. Based on the  
62 exact Mie theory and approximation formulas thereof, a number of approaches have been developed, which  
63 aim at disentangling the scattering and absorption signatures in infrared spectra of single cells. In 2008,  
64 Kohler et al. developed an algorithm based on extended multiplicative signal correction (EMSC), which  
65 corrects Mie scattering in infrared spectra of cells<sup>9</sup>. The algorithm employs an approximation formula for the  
66 extinction efficiency and takes into account a constant refractive index. Since the exact size, morphology and  
67 refractive index of a cell are unknown in all practical situations, the algorithm employs a meta-model that  
68 comprises a range of cell sizes and refractive indices. The algorithm involves several approximations. (1) It

69 considers only the extinction efficiency in forward direction when calculating the absorbance, while infrared  
70 microscopes use Schwarzschild optics and collect light over a large numerical aperture. (2) The extinction in  
71 forward direction is calculated by an approximation formula developed by V. De Hulst<sup>4</sup>. (3) The algorithm  
72 considers the refractive index as constant and real in the employed wavelength range, while it is known that  
73 for absorbing scatterers, the refractive index has a non-zero imaginary part and a fluctuating real part, i.e., is  
74 dispersive (4). The algorithm approximates the apparent absorbance by the scattering efficiency. Despite the  
75 approximations employed, the algorithm corrects the broad Mie scatter oscillations in the apparent  
76 absorbance of single cell spectra, while so-called dispersive artefacts due to the resonant Mie effect remain  
77 uncorrected. The term ‘dispersive artefact’ circumscribes the fact that absorption resonances lead to  
78 fluctuations in the real part of the refractive index, which affect the extinction efficiency and thereby the  
79 measured absorbance spectrum. In 2010, Bassan et al.<sup>6</sup> developed an iterative algorithm based on EMSC,  
80 which allows correcting the dispersive artefact. The algorithm developed by Bassan et al.<sup>6</sup> involves several  
81 approximations. (1) As in Kohler’s algorithm<sup>9</sup>, the apparent absorbance is approximated by the extinction  
82 efficiency in forward direction developed by V. de Hulst<sup>4</sup>. (2) While Bassan’s algorithm<sup>6</sup> takes into account a  
83 fluctuating real refractive index, it does not use the imaginary part of the refractive index. Recently, van de  
84 Dijk et al.<sup>10</sup> have introduced an iterative algorithm taking into account the high numerical aperture of  
85 infrared microscopes. The algorithm employs exact Mie formulas for the absorbance and treats the refractive  
86 index as complex. While it was shown that the algorithm corrects sharp dispersive Mie signatures in spectra  
87 of PMMA spheres<sup>10</sup>, it has also been demonstrated that the algorithm is not applicable to biological samples,  
88 which have a complex composition and a shape that often deviates substantially from a sphere<sup>11</sup>.

89 Although the algorithm of Bassan et al.<sup>6</sup> does not take into account a complex refractive index, it has been  
90 widely employed during recent years, since it provides a stable extraction of the pure absorbance spectrum. It  
91 is currently considered as the best existing method for correcting the Mie scatter distortions in infrared  
92 microspectroscopy of cells and tissues.

93 The aim of the present paper is to further develop the algorithm by Bassan et al.<sup>6</sup> by taking into account a  
94 complex refractive index according to Mie theory. The algorithm of Bassan et al.<sup>6</sup> requires the calculation of  
95 the Kramers-Kronig transform iteratively. Since this turns out to be a very time consuming process, we  
96 further aimed at improving the speed of the algorithm. In order to test the newly developed algorithm, we  
97 created a test set of apparent absorbance spectra. The test set consists of spectra that were distorted according

98 to exact Mie theory. For the creation of the test set, the optical set-up including the Schwarzschild optics  
99 with a focusing and collecting optics has been taken into account. The algorithm presented in this paper is  
100 based on the algorithm of Kohler et al.<sup>9</sup> and the algorithm of Bassan et al.<sup>6</sup> based on a meta-model taking  
101 into account a broad parameter range for parameters such as refractive index, size of the cell and effective  
102 sample thickness. While the resonant Mie scatter correction algorithm developed by Bassan et al.<sup>6</sup> uses three  
103 independent parameters for building the meta-model, we will show in the present paper that the meta-model  
104 can be set up with two independent parameters, which further improves the speed of the algorithm and the  
105 usage of memory in the modelling step.

## 106 Simulation of pure absorbance spectra

107 To validate the Mie scatter correction algorithm developed in this paper, a simulated data set of pure  
 108 absorbance spectra was created. The spectra were simulated such that the obtained absorbance spectra  
 109 resembled a matrigel spectrum of Bassan et al.<sup>6</sup>, i.e. a spectrum of an artificial base membrane consisting  
 110 mainly of proteins. The matrigel spectrum is considered as a nearly scatter-free pure absorbance spectrum. A  
 111 random number generator was used to change of heights ( $\pm 20\%$ ), and shift band positions ( $\pm 1 \text{ cm}^{-1}$ ) of peaks  
 112 by superimposing Lorentz lines for 50 spectra. This data set was divided into two data sets of 25 spectra. For  
 113 data set one, we systematically changed the amplitudes at the peaks positions 1116, 1127, 1172, 1233, 1294,  
 114 1388, 1544 and  $1648 \text{ cm}^{-1}$  by making them either higher or smaller for each respective band. For data set  
 115 two, we changed the amplitudes at the positions 1075, 1155, 1192, 1243, 1315, 1404, 1456, 1551 and  $1656$   
 116  $\text{cm}^{-1}$  by again making them either higher or smaller for each respective band. When analysing these data sets  
 117 by PCA, two clusters of samples were obtained according to the design of the simulation. The simulated  
 118 spectra are shown in Fig. 1a. The corresponding score plot for the first two PCA components is shown in  
 119 Fig. 1b. The first two components account in total for 78,3% of the variance in these data. From the  
 120 simulated pure absorbance spectra, the imaginary parts of refractive indices  $n'(\tilde{\nu})$  were calculated according  
 121 to

$$122 \quad n'(\tilde{\nu}) = \frac{A(\tilde{\nu})\ln(10)}{4\pi d_{eff}\tilde{\nu}}, \quad (1)$$

123 where  $d_{eff}$  is the effective thickness of the cell<sup>11</sup> and  $\tilde{\nu}$  is the wavenumber. The real part of the fluctuating  
 124 part of the refractive index was calculated by using the Kramers-Kronig transform

$$125 \quad n(\tilde{\nu}) = n_0 + \frac{2}{\pi} \text{P} \int_0^{\infty} \frac{s n'(s)}{s^2 - \tilde{\nu}^2} ds, \quad (2)$$

126 where  $n_0$  is the constant part of the real refractive index, P denotes the Cauchy principal value integral and  
 127  $n'$  is the imaginary part of the refractive index<sup>12</sup>.

128

## 129 Simulation of apparent absorbance spectra according to exact Mie theory

130 In order to simulate apparent absorbance spectra, exact Mie theory was used. In the simulations, the optical  
 131 setup of an infrared microscope with a numerical aperture  $NA$  was taken into account. The apparent  
 132 absorbance was calculated according to

$$133 \quad A_{app} = -\log_{10} \left( 1 - \frac{\pi a^2}{G} Q_{ext} + \frac{1}{4\pi G \tilde{\nu}^2} \int_0^{\theta_{NA}} [i_1(\theta) + i_2(\theta)] \sin(\theta) d\theta \right), \quad (3)$$

134 where  $a$  is the radius of the spherical scatterer,  $G$  is the size of the aperture and  $\tilde{\nu}$  is the wavenumber. The  
135 integration is performed over the numerical aperture  $\theta_{NA}$  with integrand functions  $i_{1,2}(\theta)$ , which are  
136 calculated from the scattering amplitudes  $S_{1,2}(\theta)$ . Details are given in the Supplementary Material S.2 of  
137 paper Lukacs et. al<sup>11</sup>. For each simulated pure absorbance spectrum (see description in the previous section),  
138 imaginary and real parts of the refractive index were calculated according to Eqs. 1 and 2 and displayed in  
139 Fig. 1c and 1d, respectively. For each simulated apparent absorbance spectrum  $A_{app}$ , random values were  
140 chosen for  $n_0$  and  $a$  from the intervals  $1.1 < n_0 < 1.4$  and  $2m\mu < a < 5.5m\mu$ . Following this procedure, a  
141 set of 50 simulated apparent absorbance spectra was obtained. The apparent absorbance spectra are shown in  
142 Fig. 1e. The score plot of the first two components of the corresponding PCA analysis is shown in Fig. 1f.  
143 We can see that due to the scatter distortions, the two groups that were observed in the score plot of the first  
144 two components of the PCA of the pure absorbance spectra (Fig.1b) are now mixed. It is important to note  
145 that visualization of score plots of higher components reveals the grouping also in the apparent absorbance  
146 spectra. This is expected, since the scatter distortions are simply leading to a distortion of the main variation  
147 pattern, but the information related to the grouping according to the chemical difference is still obtained in  
148 the simulated apparent absorbance spectra. It is important to mention that the simulated apparent absorbance  
149 spectra as shown in Fig. 1c include the so-called dispersive artefact. When the apparent absorbance spectra  
150 in Fig. 1c are corrected according to the EMSC algorithm developed by Kohler et al. <sup>9</sup>, the dispersive artefact  
151 can be clearly seen (results not shown). The dispersive artefact is due to the fluctuations of the real refractive  
152 index caused by the absorption resonances and is not corrected by the algorithm developed by Kohler et al. <sup>9</sup>,  
153 since the model assumes a real and constant refractive index.

154 We further would like to mention that the apparent absorbance spectra in Fig. 1e contain ripples which are  
155 higher frequency oscillations. Ripples can be seen clearly in the region from  $2800\text{cm}^{-1}$  to  $1800\text{cm}^{-1}$ . These  
156 ripples are also appearing in other spectral regions, but are less visible since they overlap with chemical  
157 absorbance bands. While we have observed ripples in spectra of pollen<sup>11</sup>, ripples are usually not dominant in  
158 spectra of human and animal cells and tissues.

159

160 **Extended multiplicative signal correction and meta-modelling**

161 For the extraction of the pure absorbance spectra from simulated apparent absorbance spectra, an iterative  
 162 algorithm based on EMSC was developed, which is a further extension of the algorithms presented in Kohler  
 163 et al.<sup>9</sup> and Bassan et al.<sup>7</sup>. Multiplicative signal correction (MSC) and EMSC have been introduced for pre-  
 164 processing of near-infrared spectra<sup>13, 14</sup>. It has been shown in the past that both methods are versatile tools for  
 165 correcting infrared spectra of biological materials<sup>6, 9, 15-17</sup>. When EMSC is used for estimating and correcting  
 166 Mie scattering, a measured absorbance spectrum  $A_{app}(\tilde{\nu})$  is approximated by a reference spectrum  $Z_{ref}(\tilde{\nu})$   
 167 times a multiplicative effect  $b$ , plus deviations from this reference spectrum expressed by a constant baseline  
 168  $c$  plus a sum of components  $p_i(\tilde{\nu})$  times respective parameters  $g_i$

$$169 \quad A_{app}(\tilde{\nu}) = bZ_{ref}(\tilde{\nu}) + c + \sum_{i=1}^{A_{opt}} g_i p_i(\tilde{\nu}) + \varepsilon(\tilde{\nu}). \quad (4)$$

170 The un-modelled part is captured by the residual term  $\varepsilon(\tilde{\nu})$ . Further baseline effects may be included in the  
 171 model by adding polynomials to the EMSC model<sup>15, 16</sup>. Since EMSC models an apparent absorbance  
 172 spectrum around a reference spectrum, the estimation of the model parameter has turned out to be a very  
 173 stable process. This is because infrared spectra of biological materials have very similar spectral signatures  
 174 deriving from protein, fat and carbohydrate absorptions, leading to a visually very similar overall shape of  
 175 the spectrum. When the parameters are estimated according to Eq. 4, the apparent absorbance spectrum is  
 176 corrected according to

$$177 \quad A_{corr}(\tilde{\nu}) = \frac{(A_{app}(\tilde{\nu}) - c - \sum_{i=1}^{A_{opt}} g_i p_i(\tilde{\nu}))}{b}. \quad (5)$$

178 In an EMSC Mie model, the component spectra  $p_i(\tilde{\nu})$  are obtained from a meta-model based on Mie theory.  
 179 In the meta-model used by Kohler et al.<sup>9</sup> and Bassan et al.<sup>7</sup>, the scatter extinction was approximated by the  
 180 formula derived by Van de Hulst<sup>4</sup>, which was originally developed for a constant and real refractive index  
 181 and writes as

$$182 \quad Q_{ext}(\tilde{\nu}) \approx 2 - \frac{4}{\rho} \sin \rho + \left(\frac{4}{\rho^2}\right) (1 - \cos \rho), \quad (6)$$

183 where  $\rho$  is given by

$$\rho = 4\pi a \tilde{\nu} (n - 1) \quad (7)$$

184 and  $a$  and  $n$  are the radius of the spherical particle and the real refractive index, respectively. In order to  
 185 allow for the correction of the dispersive artefact, Bassan et al.<sup>7</sup> introduced in Eq. 6 for  $n$  a non-constant real  
 186 refractive index, which was calculated from an estimate of the pure absorbance according to the Kramers-

187 Kronig transform (Eq. 2), while the imaginary part  $n'(\tilde{\nu})$  of the refractive index may be calculated from an  
188 estimate of the pure absorbance spectrum  $A(\tilde{\nu})$  according to Eq. 1. This relation was simplified in Bassan et  
189 al.<sup>7</sup> assuming that the imaginary part  $n'(\tilde{\nu})$  of the refractive index is proportional to the absorbance  $A(\tilde{\nu})$ ,  
190 i.e.

$$191 \quad n'(\tilde{\nu}) \approx s \cdot A(\tilde{\nu}) \quad (8)$$

192 where  $s$  is a proportionality factor. The proportionality is only a rough approximation since the wavenumber  
193 varies on the range under consideration. When the imaginary part of the refractive index,  $n'(\tilde{\nu})$ , is known,  
194 the real part,  $n(\tilde{\nu})$ , can be calculated according to the Kramers-Kronig relation in Eq. 2.

195

196 ***The iterative algorithm developed by Bassan et al. works as follows:***

197 The algorithm of Bassan corrects a scatter distorted apparent absorbance spectrum  $A_{app}(\tilde{\nu})$  according the  
198 following iterative procedure, which is based on the EMSC model in Eq. 4.

199 *Initialization:* Eq. 4 requires the initialization of a reference spectrum  $Z_{ref}(\tilde{\nu})$ , which ideally should be  
200 closed to the pure absorbance spectrum. To initialize the algorithm, a matrigel spectrum<sup>6</sup> was used as pure  
201 absorbance spectrum  $A(\tilde{\nu})$ .

202 *Iterative algorithm:*

- 203 1. The reference spectrum  $Z_{ref}(\tilde{\nu})$  in Eq. 4 is replaced by an estimate of the pure absorbance spectrum.
- 204 2. The estimate of the pure absorbance spectrum is further used to calculate the imaginary part of the  
205 refractive index  $n'(\tilde{\nu})$  according to Eq. 1., From the imaginary part of the refractive index  $n'(\tilde{\nu})$ , the  
206 real part of the refractive index,  $n(\tilde{\nu})$ , is calculated by the Kramers-Kronig transform according to  
207 Eq. 2. The real part of the refractive index is then used to calculate the extinction efficiency  $Q_{ext}(\tilde{\nu})$   
208 according to Eq. 3 for a wide range of parameters  $a$ ,  $n_0$  and the proportionality factor of Eq. 8,  
209 denoted by  $s$ . For each parameter typically its range is covered by 10 different values. The apparent  
210 absorbance  $A_{app}(\tilde{\nu})$  is then calculated for the range of parameters  $a$ ,  $n_0$  and  $s$  by assuming that  
211  $A_{app}(\tilde{\nu}) \approx Q_{ext}(\tilde{\nu})$ , resulting in a set of  $10 \times 10 \times 10 = 1000$  apparent absorbance spectra.

- 212 3. The set of apparent absorbance spectra  $A_{app}(\tilde{\nu})$  is approximated by a meta-model using PCA,  
 213 resulting in a set of principal components  $p_i(\tilde{\nu})$  that are used as components in Eq. 4. The EMSC  
 214 parameters in Eq. 4 are estimated by ordinary least square fits. After estimation of the EMSC  
 215 parameters, the spectrum is corrected according to Eq. 5, resulting in a corrected spectrum  $A_{corr}(\tilde{\nu})$ .  
 216 4. The estimate of the pure absorbance spectrum is replaced by the corrected spectrum  $A_{corr}(\tilde{\nu})$  and  
 217 the algorithm is reiterated starting with step 1.

218 The iterative algorithm by Bassan et al.<sup>6</sup> deserves some comments. It is important to mention that the  
 219 assumed proportionality  $A_{app}(\tilde{\nu}) \sim Q_{ext}(\tilde{\nu})$  that is employed in step 1, is a rough approximation of Eq. 3<sup>11</sup>. It  
 220 involves neglecting the third term in Eq. 3 resulting in

$$221 \quad A_{app} = -\log_{10}\left(1 - \frac{\pi a^2}{G} Q_{ext}\right) \quad (9)$$

222 where  $a$  is the radius of the sphere and  $G$  is the detector area, and further the expansion of the logarithm of  
 223 Eq. 9 up to linear order, resulting in

$$224 \quad A_{app} \approx \frac{\pi a^2}{G} Q_{ext}, \quad (10)$$

225 explaining the proportionality between  $A_{app}(\tilde{\nu})$  and  $Q_{ext}(\tilde{\nu})$ .

226

### 227 **Improved algorithm suggested in this paper.**

228 The iterative algorithm suggested in this paper involves several improvements. First, the iterative algorithm  
 229 in this paper is based on a meta-model, which involves a complex refractive index according to the Mie  
 230 theory. We used an approximation formula for the extinction efficiency, that has been derived by Van de  
 231 Hulst<sup>4</sup>

$$232 \quad Q_{ext}(\tilde{\nu}) \approx 2 - 4e^{-\rho \tan \beta} \frac{\cos \beta}{\rho} \sin(\rho - \beta) - 4e^{-\rho \tan \beta} \left(\frac{\cos \beta}{\rho}\right)^2 \cos(\rho - 2\beta) \\
 + 4 \left(\frac{\cos \beta}{\rho}\right)^2 \cos(2\beta) \quad (11)$$

232 with

$$233 \quad \rho = 4\pi a \tilde{\nu} (n - 1) \quad \text{and} \quad \tan \beta = n' / (n - 1) \quad (12)$$

234 where  $n$  and  $n'$  are the real and the imaginary parts of the refractive index, respectively. The differences  
 235 between Eq. 6 and Eq. 11 are illustrated in<sup>11</sup>. The differences are significant, both with respect to the position  
 236 of the band and the absolute values of the estimated extinction and absorbance.

237 The second improvement relates to the complexity of the meta-model. While in Bassan et al.<sup>6</sup> a parameter  
 238 model was used including ranges of three parameters (3 dimensions), it can be shown that a 2-dimensional  
 239 parameter model is sufficient for the parameter estimation. Details about the reduction from the 3-parameter  
 240 model to the 2-parameter model are given in the appendix A. The application of a 2-dimensional parameter  
 241 model decreases the computation time and required of computer memory. This can be illustrated by an  
 242 example. When the three parameter ranges represented by the size of the cell, the background refractive  
 243 index and the scaling parameter  $s$  of Eq. 8 are covered and 10 values are used to cover each parameter range,  
 244 1000 Mie extinction curves need to be simulated and used for the establishment of the meta-model.  
 245 Employing a two-parameter model, 100 spectra are sufficient to cover the same range. Thus, memory usage  
 246 is reduced by a factor 10 and the computation time for establishment of the meta-model is reduced as well.

247 A third improvement of the algorithm was achieved by speeding up the Kramers-Kronig transform of Eq. 2.  
 248 Kramers-Kronig relations are mainly used in optical spectroscopy to determine the complex refractive index  
 249  $\hat{n} = n + in'$  of the medium from the measured absorption, transmission or reflection spectrum. The  
 250 refractive index is an important quantity when considering the scattering and absorption of light at biological  
 251 materials. The real part  $n$  of this index describes the refractive properties of the material; the imaginary part  
 252  $n'$  of it, determines the absorptive properties of the material. The most employed method for obtaining  $n$   
 253 from  $n'$  and vice versa is the Kramers-Kronig transform, which expresses the real part  $n$  in terms of the  
 254 imaginary part  $n'$  according to

$$n(\tilde{\nu}) = \frac{2}{\pi} P \int_0^{+\infty} \frac{s \cdot n'(s)}{s^2 - \tilde{\nu}^2} ds, (13a)$$

255 and the imaginary part  $n'$  in terms of the real part  $n$  by

$$n'(\tilde{\nu}) = -\frac{2\tilde{\nu}}{\pi} P \int_0^{+\infty} \frac{n(s)}{s^2 - \tilde{\nu}^2} ds. (13b)$$

256 In Appendix B, we show that these relations are equivalent to the Hilbert transform, since the real part of the  
 257 refractive index is an even function of the wavenumber and the imaginary part of the refractive index is an  
 258 odd function of wavenumber, i.e.  $n(\tilde{\nu}) = n(-\tilde{\nu})$  and  $n'(\tilde{\nu}) = -n'(-\tilde{\nu})$ . This can be seen from the Lorentz  
 259 model. Details are given in Supplementary Material S.1 of reference<sup>11</sup>. The Hilbert transform writes as

$$n(\tilde{\nu}) = \frac{1}{\pi} P \int_{-\infty}^{+\infty} \frac{n'(s)}{s - \tilde{\nu}} ds = -\frac{1}{\pi\tilde{\nu}} * n'(\tilde{\nu}) \quad (14a)$$

260 and

$$n'(\tilde{\nu}) = -\frac{1}{\pi} P \int_0^{+\infty} \frac{n(s)}{s - \tilde{\nu}} ds = \frac{1}{\pi\tilde{\nu}} * n(\tilde{\nu}) \quad (14b)$$

261 respectively, where \* denotes convolution. The Hilbert transform can be calculated via Fast Fourier  
 262 Transform (FFT). The FFT method is based on the fact that both real and imaginary parts of the complex  
 263 refractive index defining the Hilbert transform are proportional to the convolution product between  $n(\tilde{\nu})$  or  
 264  $n'(\tilde{\nu})$  and the convolution kernel function  $\frac{1}{\pi\tilde{\nu}}$ . In Eqs. 14 there is a singularity, when  $s$  is equal to  $\tilde{\nu}$ . The  
 265 singularity problem is theoretically bypassed by introducing the Cauchy Principal Value<sup>18</sup>.

266

267 ***The new iterative algorithm works as follows:***

268 The algorithm corrects a scatter distorted apparent absorbance spectrum  $A_{app}(\tilde{\nu})$  according to the following  
 269 iterative procedure which is based on the EMSC model in Eq. 4.

270 *Initialization:* The reference spectrum  $Z_{ref}(\tilde{\nu})$  in Eq. 4 is initialized by a matrigel spectrum<sup>6</sup> or another  
 271 appropriate non-distorted spectrum.

272 *Iterative algorithm:*

- 273 1. The reference spectrum  $Z_{ref}(\tilde{\nu})$  in Eq. 4 may be either updated<sup>6</sup> or the same reference spectrum may  
 274 be used in each iteration.
- 275 2. The estimate of the pure absorbance spectrum is further used to calculate the imaginary part of the  
 276 refractive index  $n'(\tilde{\nu})$  according to Eq. 1. The real part of the refractive index,  $n(\tilde{\nu})$ , is calculated  
 277 from the imaginary part of the refractive index,  $n'(\tilde{\nu})$ , by the Hilbert transform (function Hilbert in  
 278 Matlab) according to Eq. 14a. The calculations of the Hilbert function are based on the FFT  
 279 algorithm. The real part of the refractive index is then used to calculate the extinction efficiency  
 280  $Q_{ext}(\tilde{\nu})$  according to Eq. 11 involving a complex refractive index. In order to cover the relevant  
 281 parameter range, the scaled parameters  $\gamma$  and  $\alpha_0$  according to Eqs. A20 and A21 are used (see  
 282 Appendix A) with the ranges  $\alpha_0 \in [0.2 \mu\text{m}, 2.2 \mu\text{m}] \cdot 4\pi$  and  $\gamma \in [5 \cdot 10^4 \frac{1}{\text{m}}, 6 \cdot 10^5 \frac{1}{\text{m}}]$ . The  
 283 corresponding ranges of  $n_0$ ,  $a$  and  $f$  are given in A13. A set of 50 apparent absorbance  $A_{app}(\tilde{\nu})$  is

284 then calculated according to Eq. 9 uniformly covering the parameter ranges for  $\alpha_0$  and  $\gamma$ , and stored  
285 as rows in a matrix  $M$ .

- 286 3. The set of apparent absorbance spectra  $A_{app}(\tilde{\nu})$ , i.e. the matrix  $M$  is approximated by a meta-model  
287 using PCA resulting in a set of principal components  $p_i(\tilde{\nu})$  that are used as components in Eq. 4.  
288 Prior to approximation by PCA, the matrix  $M$  is orthogonalized with respect to the reference  
289 spectrum  $Z_{ref}(\tilde{\nu})$ . This is to avoid competition between the parameters  $b$  and  $g_i$  (see Eq. 4) in the  
290 subsequent parameter estimation. The EMSC parameters in Eq. 4 are estimated by ordinary least  
291 squares fits. After estimation of the EMSC parameters, the spectrum is corrected according to Eq. 5  
292 resulting in a corrected spectrum  $A_{corr}(\tilde{\nu})$ .
- 293 4. The estimate of the pure absorbance spectrum is replaced by the corrected spectrum  $A_{corr}(\tilde{\nu})$  and  
294 the algorithm is reiterated starting with step 1.

295 This iterative algorithm is described schematically in Fig. 2. We suggest to call the algorithm fast  
296 resonant Mie scatter correction.

### 297 **EMSC correction of simulated and measured apparent absorbance spectra**

298 The correction of an apparent absorbance spectrum according to the algorithm suggested in this paper is  
299 demonstrated in Fig. 3. In Fig. 3a an example of a simulated apparent absorbance spectrum is shown. The  
300 spectrum is simulated employing Eq. 3. As parameters we used  $n_0 = 1.35$  and  $a = 3.81 \mu\text{m}$ . Corrected  
301 spectra that were obtained by the first three iterations of the correction algorithm proposed in this paper are  
302 shown in Fig. 3b together with the reference spectrum and the pure absorbance spectrum. As a reference  
303 spectrum we used the average spectrum of all simulated pure absorbance spectra. Alternatively, the matrigel  
304 spectrum could be used. It can be seen that the algorithm converges quickly and that the corrected spectra are  
305 close to the pure absorbance spectra used for the simulation. Ripples that can be observed in the region  
306 between  $4000 \text{ cm}^{-1}$  and  $3500 \text{ cm}^{-1}$  were not corrected successfully. This is expected, since the Van de Hulst  
307 formula used for the correction (see Eq. 11) does not describe the Mie ripples. In Fig. 4a, a simulated  
308 apparent absorbance spectrum containing strong ripples is shown. As parameters, we used  $n_0 = 1.36$  and  
309  $a = 5.12 \mu\text{m}$ . Ripples with these intensities are usually not observed in infrared microspectroscopy of single  
310 cells. An explanation for this will be given elsewhere. In the corrected spectra in Fig. 4b it can be seen  
311 clearly that the Van De Hulst algorithm is not capable of correcting the ripples.

312 The complete set of corrected spectra for the simulated apparent absorbance spectra from Fig. 1e is shown in  
313 Fig. 5. The spectra that correspond to the red scores of the pure absorbance spectra in Fig. 1b are plotted red  
314 in Fig. 5, while the spectra that correspond to the blue scores of the pure absorbance spectra in Fig. 1b are  
315 plotted blue in Fig. 5. The reference spectrum is shown in green. It can be seen that the correction of the  
316 spectra worked well. The two groups of spectra can be separated visually after correction. As mentioned  
317 before, ripples are not well corrected, which does not pose a major problem, since strong ripples are usually  
318 not observed in the infrared microspectroscopy of single cells. The computation time for the correction of 50  
319 spectra (one iteration in the iterative algorithm) using a 4th generation Intel® Core™ i7-4702HQ quad core  
320 processor, 16GB memory and Matlab 2015 is 77 seconds. This is a substantial improvement to the algorithm  
321 developed by Bassan et al.<sup>6</sup> which uses 765 seconds on the same computer (employing numerical integration  
322 and a parameter model with 3 parameters). No speed optimization of the algorithm by vectorization or  
323 parallel programming was done so far. It is important to mention that the Kramers-Kronig part of the  
324 algorithm is improved by a factor of approximately 200 when using the algorithm based on the Hilbert  
325 transform compared to the numerical integration. The improvement of the Kramers-Kronig part shows  
326 especially advantages when more than 1 iterations are applied in the iterative algorithm.

327 In order to demonstrate that chemical information that was distorted in the apparent absorbance spectra can  
328 be restored, we investigated peak ratios before and after correction. In Fig. 6, the peak ratios for the  
329 simulated pure absorbance spectra of the band at  $1546\text{ cm}^{-1}$  and the band at  $1387\text{ cm}^{-1}$  are shown in blue. The  
330 peak ratio of this band is simulated such that the 50 spectra can be clearly separated into two groups of 25  
331 spectra each. The spectra 1-25 have a lower peak ratio than the spectra 26-50. The corresponding peak ratios  
332 for the apparent absorbance spectra are shown in magenta. It is obvious that the scatter distorted apparent  
333 absorbance spectra do not allow to separate these two groups with the help of the peak ratio of the band at  
334  $1546\text{ cm}^{-1}$  and the band at  $1387\text{ cm}^{-1}$ . The apparent absorbance spectra were then corrected by the iterative  
335 algorithm. Corrected spectra are shown in red (one iteration), green (two iterations) and black (three  
336 iterations). The ratio obtained from the average spectrum of all simulated pure absorbance spectra that was  
337 used as the reference spectrum for the EMSC model is shown as the blue dashed line for comparison. It can  
338 be seen that the iterative algorithm retrieves a good estimation of the ratio of the simulated pure absorbance  
339 spectrum.

340 We further tested the algorithm on a set of measured infrared microspectroscopy spectra of lung cancer cells.  
341 Details about the data set can be found in Kohler et al.<sup>9</sup>. The measured spectra are shown in Fig. 7 (red)  
342 together with the corrected spectra (green). For the correction one iteration step was used. As reference  
343 spectrum the matrigel spectrum was used<sup>6</sup>. In Fig. 7, it can be seen that correction works visually very well.  
344 The resonant Mie effect that was not corrected by the algorithm presented in Kohler et al.<sup>9</sup>, is now  
345 successfully corrected.

346

### 347 **The importance of the reference spectrum for the iterative algorithm**

348 An important comment relates to the updating of the EMSC reference spectrum in the iterative algorithm.  
349 The dashed line in Fig. 2 indicates, that there are two options: Either the reference spectrum is updated by the  
350 new estimate of the pure absorbance spectrum obtained after each iteration or the initial reference spectrum  
351 is kept and only the imaginary part of the refractive index and, after Kramers-Kronig transformation, the real  
352 part of the refractive index are updated. We have observed that an update of the reference spectrum may lead  
353 to instabilities in the iterative algorithm and the result obtained may completely depend on the number of  
354 iterations used, i.e. the iterative algorithm may drift completely apart from reasonable solutions. Thus, we do  
355 not suggest to update the reference spectrum for EMSC in the iterative algorithm.

356 The use of a good reference spectrum is crucial for the success of the correction algorithm. In Fig.7 it is  
357 obvious that the corrected spectra become in their overall shape very close to the reference spectrum. This  
358 can be clearly seen when comparing the reference spectrum (for example in Fig. 4b) with the corrected  
359 spectra in Fig. 7. The same observation can be made in the paper of Bassan et al.<sup>6</sup>, where the same reference  
360 spectrum was used as in the current paper. In reference<sup>6</sup>, after correction all spectra are in their overall shape  
361 similar to the matrigel spectrum used as a reference in EMSC. This is due to the high flexibility of the meta-  
362 model used for the correction. Notwithstanding, although the corrected spectra tend overall in their shape  
363 towards the reference spectrum, we could clearly show that chemical information can be restored by the  
364 suggested algorithm.

365

### 366 **Conclusions**

367 In this work we presented an improved iterative EMSC algorithm for correcting Mie scattering in infrared  
368 microspectroscopy of single cells and tissues. The iterative EMSC algorithm employs a meta-model based on

369 an approximate formula by Van De Hulst, taking into account a complex refractive index for correcting Mie  
370 scattering. The new iterative algorithm was tested using a simulated set of apparent absorbance spectra and a  
371 set of measured apparent absorbance spectra. The simulated apparent absorbance spectra were obtained by  
372 first simulating pure absorbance spectra and then generating scatter distorted apparent absorbance spectra by  
373 full Mie theory. For the simulations, the full optical set up of an infrared microscope including the collecting  
374 and focusing Schwarzschild optics were taken into account. The set of simulated spectra used in this paper is  
375 thus more difficult to correct than the spectra simulated in the reference<sup>6</sup>, where spectra were simulated by  
376 using exactly the same approximation formula that was afterwards used for correction algorithm. In addition,  
377 the spectra simulated in reference<sup>6</sup> were obtained by addition of pure absorbance spectra to simulated scatter  
378 spectra. This facilitated the correction of the spectra in reference<sup>6</sup>, since scatter distortions were only added  
379 on top of the pure absorbance spectra. In our simulations the scatter distorted spectra were obtained  
380 according to Eq. 3 and do not contain additive contributions of pure absorbance spectra. It is important to  
381 mention that according to the Mie theory, apparent absorbance spectra are not obtained by adding pure  
382 absorbance spectra to scatter contributions. Thus, the retrieval of chemical information from the simulated  
383 apparent absorbance spectra taking into account the full optical setup as employed in the current paper,  
384 demonstrates well the capability of the algorithm presented in this paper.

385 The measured spectra used for correction in the current paper were obtained from single lung cancer cells<sup>9</sup>.  
386 The correction of the measured spectra was successful, while it is obvious that the corrected spectra tend in  
387 their overall shape towards the matrigel spectrum employed. The high flexibility of the meta-model results in  
388 corrected spectra that are in their overall shape very similar to the reference spectrum used in the EMSC  
389 model, while we showed by employing a simulated data set that chemical characteristics of the pure  
390 absorbance spectra could be restored.

391 The iterative algorithm developed by Bassan et al.<sup>6</sup> involves a numerical integration in order to perform a  
392 Kramers-Kronig transform. In the algorithm presented in this paper, we replaced the integral of the Kramers-  
393 Kronig by a fast Fourier transform (FFT) algorithm. This reduced the computation time of the Kramers-  
394 Kronig transform approximately by a factor 100. Moreover we have shown that two independent parameters  
395  $\alpha_0$  and  $\gamma$  (each parameter contains 10 equidistant values in its respective range) are sufficient for  
396 compressing 100 Mie scattering curves into a small number of principal components loading spectra to  
397 estimate the scattering contributions in the EMSC meta-model.

398 While we have shown that the new algorithm retrieves the pure absorbance spectra from highly distorted  
 399 apparent absorbance spectra, ripples that are present in simulated apparent absorbance spectra could not be  
 400 corrected, since the Van de Hulst approximation does not account for ripples. The ripples that are visible in  
 401 the simulated apparent absorbance spectra can be explained by diffractive surface waves. While we have  
 402 observed that the appearance of ripples is not present or suppressed in measured spectra, we believe that the  
 403 correction of ripples is in general not required for the correction of infrared microspectroscopic spectra of  
 404 single cells and tissues. Ripples may be absent in measured spectra because the apertures used in infrared  
 405 microspectroscopy are comparable to the size of the cells, while the exact Mie theory which assumes an  
 406 incoming plane wave assumes apertures that are much bigger than the probed cell. Thus, diffractive surface  
 407 waves that are causing ripples in exact Mie theory may be suppressed in practical measurement situations.

408

#### 409 *Acknowledgements*

410 The authors wish to thank Peter Gardener and Paul Bassan for providing the matrigel and Josep Sule Suso  
 411 for providing the set of measured lung cancer cell spectra.

412

### 413 **Appendix A: Complexity of meta model**

414 For building a meta-model we take into account a suitable parameter space for the approximation formula  
 415 employed for the extinction efficiency. The approximation formula given by Eq. 11 contains the parameters  
 416  $\rho$  and  $\beta$ . We define

$$417 \quad \alpha = 4\pi a(n - 1), \quad (\text{A1})$$

418 where  $n$  is the real refractive index and  $a$  is the size of the sphere. It follows that  $\rho = \tilde{\nu}\alpha$ .

419 When the pure absorbance spectrum  $A(\tilde{\nu})$  is known, the imaginary part of the refractive index can be  
 420 calculated according to

$$421 \quad n'(\tilde{\nu}) = \frac{A(\tilde{\nu})\ln(10)}{4\pi d_{eff}\tilde{\nu}}, \quad (\text{A2})$$

422 where  $d_{eff}$  is the effective thickness of the cell<sup>11</sup>. The real part of the refractive index  $n(\tilde{\nu})$  can then be  
 423 calculated by the Kramers-Kronig relation according to

$$424 \quad n(\tilde{\nu}) = n_0 + \frac{2}{\pi} \mathbf{P} \int_0^\infty \frac{s \cdot n'(s)}{s^2 - \tilde{\nu}^2} ds, \quad (\text{A3})$$

425 where  $n_0$  is the constant part of the real refractive index and the integral term

$$426 \quad n_{kk}(\tilde{\nu}) = \frac{2}{\pi} P \int_0^\infty \frac{s \cdot n'(s)}{s^2 - \tilde{\nu}^2} ds \quad (\text{A4})$$

427 is the fluctuating part of the real refractive index.

428 It follows that

$$429 \quad \alpha = 4\pi a(n_0 + n_{kk} - 1). \quad (\text{A5})$$

430 If  $n_{kk}$  is calculated from the pure absorbance spectrum  $A(\tilde{\nu})$  according to Eqs. A2 and A4, the effective  
431 thickness  $d_{eff}$  of the cell is in general not known. We therefore define a scaled imaginary part of the  
432 refractive index,  $n'_s(\tilde{\nu})$ , according to

$$433 \quad n'_s(\tilde{\nu}) = \frac{A(\tilde{\nu})}{\tilde{\nu}}, \quad (\text{A6})$$

434 where

$$435 \quad n'(\tilde{\nu}) = f n'_s(\tilde{\nu}), \quad (\text{A7})$$

436 with the scaling constant

$$437 \quad f = \frac{\ln(10)}{4\pi d_{eff}}. \quad (\text{A8})$$

438 The fluctuating part is consequently calculated according to

$$439 \quad n_{kk}(\tilde{\nu}) = f n_{kk,s}(\tilde{\nu}) \quad (\text{A9})$$

440 where

$$441 \quad n_{kk,s}(\tilde{\nu}) = \frac{2}{\pi} P \int_0^\infty \frac{s \cdot n'_s}{s^2 - \tilde{\nu}^2} ds. \quad (\text{A10})$$

442 Thus, we obtain

$$443 \quad \alpha = 4\pi a(n_0 + f n_{kk,s} - 1) \quad (\text{A11})$$

444 and

$$445 \quad \tan\beta = \frac{fn'_s}{n_0 + fn_{kk,s} - 1}. \quad (\text{A12})$$

446 Generally the exact numbers for  $a$ ,  $n_0$  and  $f$  are not known. Only ranges for these values can be given.

447 These parameters have to be estimated in the modeling process. The following ranges were found to be

448 optimal

$$449 \quad n_0 \in [1.1, 1.4], \quad (\text{A13a})$$

$$450 \quad f \in \left[10^4 \frac{1}{m}, 3 \cdot 10^4 \frac{1}{m}\right], \quad (\text{A13b})$$

$$451 \quad a \in [2\mu\text{m}, 5.5\mu\text{m}]. \quad (\text{A13c})$$

452 Since the parameters  $a$  and  $n_0$  are not independent (see A5), these parameter ranges are not absolute. We

453 include for example considerably higher values of  $a$  than indicated by the range in (A13c), when the

454 refractive index in an apparent absorbance spectrum is below the maximum value of (A13a), since the two

455 parameters enter Eq. A5 as a product. The parameters in Eqs. A13 are not independent and one parameter

456 can be omitted by rescaling as we will show in the following. We can write Eq. A11 as

$$457 \quad \alpha = 4\pi a(n_0 - 1) \left(1 + \frac{fn_{kk,s}}{(n_0 - 1)}\right), \quad (\text{A14})$$

458 and Eq. A12 as

$$459 \quad \tan\beta = \frac{n'_s}{\frac{n_0 - 1}{f} + n_{kk,s}}. \quad (\text{A15})$$

460 By defining

$$461 \quad \alpha_0 = 4\pi a(n_0 - 1), \quad (\text{A16})$$

462 and

$$463 \quad \gamma = \frac{f}{(n_0 - 1)}, \quad (\text{A17})$$

464 we obtain

$$465 \quad \alpha = \alpha_0(1 + \gamma n_{kk,s}), \quad (\text{A18})$$

466 and

$$467 \quad \tan\beta = \frac{n'_s}{1/\gamma + n_{kk,s}} \quad (\text{A19})$$

468 with the respective ranges that correspond to the values in Eqs.A13:

$$469 \quad \gamma \in \left[ 5 \cdot 10^4 \frac{1}{\text{m}}, 6 \cdot 10^5 \frac{1}{\text{m}} \right] \quad (\text{A20})$$

$$470 \quad \alpha_0 \in [0.2\mu\text{m}, 2.2\mu\text{m}] \cdot 4\pi \quad (\text{A21})$$

471 It follows that the obtained model contains two independent parameters  $\gamma$  and  $\alpha_0$ . The parameter  $\gamma$  is the  
 472 new scaling value for the non-constant refractive index. A correct estimate of this parameter is important for  
 473 the biochemical interpretation of the FTIR spectra. The parameter  $\alpha_0$  corresponds to the  $\alpha$ -value of the non-  
 474 resonant case used in Kohler et al<sup>9</sup>. A good estimation of the  $\alpha_0$ -value is important for the estimation of the  
 475 physical parameters as size of cells  $a$  and constant part of the real refractive index  $n_0$ .

## 476 **Appendix B: Hilbert transform and Kramers-Kronig relations for a calculation** 477 **of the complex refractive index**

478 In order to define the complex refractive index  $\hat{n}(\tilde{\nu}) = n(\tilde{\nu}) + in'(\tilde{\nu})$  of materials from measured  
 479 absorption, transmission or reflection spectra in optical spectroscopy, Kramers-Kronig relations are used.  
 480 The complex refractive index is an important physical quantity when considering the scattering and  
 481 absorption of infrared light at biological materials. The real part  $n(\tilde{\nu})$  of this index describes the refractive  
 482 properties of the material; the imaginary part  $n'(\tilde{\nu})$  of it determines the absorptive properties of the material.  
 483 A method for obtaining  $n(\tilde{\nu})$  and  $n'(\tilde{\nu})$  is the Kramers-Kronig transform, which relates the real part  $n(\tilde{\nu})$  to  
 484 the imaginary part  $n'(\tilde{\nu})$  of the complex refractive index:

$$n(\tilde{\nu}) = \frac{2}{\pi} P \int_0^{+\infty} \frac{s \cdot n'(s)}{s^2 - \tilde{\nu}^2} ds, \quad (\text{B1a})$$

$$n'(\tilde{\nu}) = -\frac{2\tilde{\nu}}{\pi} P \int_0^{+\infty} \frac{n(s)}{s^2 - \tilde{\nu}^2} ds, \quad (\text{B1b})$$

485 where  $P$  denotes Cauchy's Principal Value.

486 These relations are equivalent to the Hilbert transform, provided that the real part is an even function of  
 487 wavenumber and the imaginary part is an odd function of wavenumber, i.e.  $n(\tilde{\nu}) = n(-\tilde{\nu})$  and  $n'(\tilde{\nu}) =$   
 488  $-n'(-\tilde{\nu})$ :

$$n(\tilde{\nu}) = \frac{1}{\pi} P \int_{-\infty}^{+\infty} \frac{n'(s)}{s - \tilde{\nu}} ds = -\frac{1}{\pi \tilde{\nu}} * n'(\tilde{\nu}), \quad (\text{B2a})$$

$$n'(\tilde{\nu}) = -\frac{1}{\pi} P \int_{-\infty}^{+\infty} \frac{n(s)}{s - \tilde{\nu}} ds = \frac{1}{\pi \tilde{\nu}} * n(\tilde{\nu}). \quad (\text{B2b})$$

489 Let us consider the connections between Eqs. B1 and B2. Because of  $n'(\tilde{\nu})$  is an odd function of  
 490 wavenumber, this property permits the conversion of the Hilbert transform pair (Eq.B2a) into the Kramers-  
 491 Kronig relations. The Hilbert transform pair (Eq.B2a) is expanded as

$$n(\tilde{\nu}) = \frac{1}{\pi} P \int_{-\infty}^{+\infty} \frac{n'(s)}{s - \tilde{\nu}} ds = \frac{1}{\pi} P \int_{-\infty}^0 \frac{n'(s)}{s - \tilde{\nu}} ds + \frac{1}{\pi} P \int_0^{+\infty} \frac{n'(s)}{s - \tilde{\nu}} ds$$

492 with  $n'(\tilde{\nu}) = -n'(-\tilde{\nu})$  we get

$$n(\tilde{\nu}) = \frac{1}{\pi} P \int_0^{+\infty} \frac{n'(s)}{s + \tilde{\nu}} ds + \frac{1}{\pi} P \int_0^{+\infty} \frac{n'(s)}{s - \tilde{\nu}} ds = \frac{2}{\pi} P \int_0^{+\infty} \frac{s \cdot n'(s)}{s^2 - \tilde{\nu}^2} ds.$$

493 Because of  $n(\tilde{\nu})$  is an even function of wavenumber, this property permits the conversion of the Hilbert  
 494 transform pair (Eq.B2b) into the Kramers-Kronig relations. The Hilbert transform pair (Eq.B2b) is expanded  
 495 as

$$n'(\tilde{\nu}) = -\frac{1}{\pi} P \int_{-\infty}^{+\infty} \frac{n(s)}{s - \tilde{\nu}} ds = -\frac{1}{\pi} P \int_{-\infty}^0 \frac{n(s)}{s - \tilde{\nu}} ds - \frac{1}{\pi} P \int_0^{+\infty} \frac{n(s)}{s - \tilde{\nu}} ds$$

496 with  $n(\tilde{\nu}) = n(-\tilde{\nu})$

$$n'(\tilde{\nu}) = \frac{1}{\pi} P \int_0^{+\infty} \frac{n(s)}{s + \tilde{\nu}} ds - \frac{1}{\pi} P \int_0^{+\infty} \frac{n(s)}{s - \tilde{\nu}} ds = -\frac{2\tilde{\nu}}{\pi} P \int_0^{+\infty} \frac{n(s)}{s^2 - \tilde{\nu}^2} ds.$$

497 The Hilbert transform can be calculated via the Fast Fourier Transform (FFT). The FFT method is based on  
 498 the fact that both real and imaginary parts of the complex refractive index defining the Hilbert transform are  
 499 proportional to the convolution product between  $n(\tilde{\nu})$  or  $n'(\tilde{\nu})$  and the convolution kernel function  $\frac{1}{\pi \tilde{\nu}}$ .

500 In Eqs. B2 there is a singularity, when  $s$  is equal to  $\tilde{\nu}$ . The singularity problem is theoretically bypassed by  
501 introducing the Cauchy Principal Value.

502 *Derivations of Hilbert transform and Kramers-Kronig relations*

503 If  $\hat{n}(\tilde{\nu})$  is an analytic function, then  $\frac{\hat{n}(s)}{s-\tilde{\nu}}$  is an analytic function too except at the pole  $s = \tilde{\nu}$ . Cauchy's  
504 theorem states that

$$\oint f(s)ds = 0,$$

505 provided that the closed contour encloses no poles of the analytic function  $f(s)$ . Let us apply Cauchy's  
506 theorem to the function  $\frac{\hat{n}(s)}{s-\tilde{\nu}}$ , where  $\tilde{\nu}$  is a point on the real axis, and the contour, shown in Fig. 8, is the union  
507 of four curves with parametric representations

508  $C_1: s = \Omega$ , where  $-R \leq \Omega \leq \tilde{\nu} - \rho$ ;

509  $C_2: s = \tilde{\nu} + \rho e^{i\varphi}$ , where  $0 \leq \varphi \leq \pi$ ;

510  $C_3: s = \Omega$ , where  $\tilde{\nu} + \rho \leq \Omega \leq R$ ;

511  $C_4: s = R e^{i\varphi}$ , where  $0 \leq \varphi \leq \pi$ .

512 From Cauchy's theorem we have

$$\int_{-R}^{\tilde{\nu}-\rho} \frac{\hat{n}(s)}{s-\tilde{\nu}} ds + \int_{\pi}^0 \frac{\hat{n}(\tilde{\nu} + \rho e^{i\varphi})}{\tilde{\nu} + \rho e^{i\varphi} - \tilde{\nu}} i\rho e^{i\varphi} d\varphi + \int_{\tilde{\nu}+\rho}^R \frac{\hat{n}(s)}{s-\tilde{\nu}} ds + \int_0^{\pi} \frac{\hat{n}(R e^{i\varphi})}{R e^{i\varphi} - \tilde{\nu}} iR e^{i\varphi} d\varphi = 0.$$

513 Therefore

$$\int_{-R}^{\tilde{\nu}-\rho} \frac{\hat{n}(s)}{s-\tilde{\nu}} ds + i \int_{\pi}^0 \hat{n}(\tilde{\nu} + \rho e^{i\varphi}) d\varphi + \int_{\tilde{\nu}+\rho}^R \frac{\hat{n}(s)}{s-\tilde{\nu}} ds + i \int_0^{\pi} \frac{\hat{n}(R e^{i\varphi})}{R e^{i\varphi} - \tilde{\nu}} R e^{i\varphi} d\varphi = 0.$$

514 Putting  $\rho \rightarrow 0$  and  $R \rightarrow \infty$ , we have

$$\lim_{\substack{\rho \rightarrow 0, \\ R \rightarrow \infty}} \left( \int_{-R}^{\tilde{\nu}-\rho} \frac{\hat{n}(s)}{s-\tilde{\nu}} ds + \int_{\tilde{\nu}+\rho}^R \frac{\hat{n}(s)}{s-\tilde{\nu}} ds + i \int_{\pi}^0 \hat{n}(\tilde{\nu} + \rho e^{i\varphi}) d\varphi + i \int_0^{\pi} \frac{\hat{n}(R e^{i\varphi})}{R e^{i\varphi} - \tilde{\nu}} R e^{i\varphi} d\varphi \right) = 0.$$

$$\lim_{\rho \rightarrow 0} \left( \int_{-\infty}^{\tilde{\nu}-\rho} \frac{\hat{n}(s)}{s-\tilde{\nu}} ds + \int_{\tilde{\nu}+\rho}^{+\infty} \frac{\hat{n}(s)}{s-\tilde{\nu}} ds \right) - i\pi \hat{n}(\tilde{\nu}) = 0.$$

515 We obtain the last line since the fourth term vanishes as  $R \rightarrow \infty$  if  $\lim_{|s| \rightarrow \infty} \hat{n}(s) = 0$ .

516 According to the definition of the Cauchy Principal Value of an integral we get

$$\lim_{\rho \rightarrow +0} \left( \int_{-\infty}^{\tilde{\nu}-\rho} \frac{\hat{n}(s)}{s-\tilde{\nu}} ds + \int_{\tilde{\nu}+\rho}^{+\infty} \frac{\hat{n}(s)}{s-\tilde{\nu}} ds \right) = P \int_{-\infty}^{+\infty} \frac{\hat{n}(s)}{s-\tilde{\nu}} ds, \quad (1)$$

517 and therefore, from (1), we have

$$\frac{1}{\pi i} P \int_{-\infty}^{+\infty} \frac{\hat{n}(s)}{s-\tilde{\nu}} ds = \hat{n}(\tilde{\nu}).$$

518 Taking the real and imaginary parts of  $\hat{n}(\tilde{\nu}) = n(\tilde{\nu}) + in'(\tilde{\nu})$ , we get

$$H[n(\tilde{\nu})] = n'(\tilde{\nu}) = -\frac{1}{\pi} P \int_{-\infty}^{+\infty} \frac{n(s)}{s-\tilde{\nu}} ds,$$

$$H^{-1}[n'(\tilde{\nu})] = n(\tilde{\nu}) = \frac{1}{\pi} P \int_{-\infty}^{+\infty} \frac{n'(s)}{s-\tilde{\nu}} ds.$$

519 The last two expressions are called the *Hilbert transform pair*.

520 Now we focus on the numerical solution of the Hilbert transform pair.

521 By means of the Fourier transform definition an analytic signal  $x(t)$  can be represented in the following way

$$x(t) = F^{-1}[X(f)] = \int_{-\infty}^{+\infty} X(f) \exp(i2\pi ft) df,$$

522 where

$$X(f) = F[x(t)] = \int_{-\infty}^{+\infty} x(t) \exp(-i2\pi ft) dt.$$

523 According to the definition of the Hilbert transform for a function  $x(t)$  we have

$$\tilde{x}(t) = H(x(t)) = \frac{1}{\pi} P \int_{-\infty}^{+\infty} \frac{x(s)}{s-t} ds = \frac{1}{\pi t} * x(t).$$

524 Since

$$F\left(\frac{1}{\pi t}\right) = -i[\text{sign}(f)] = \begin{cases} -i, & f > 0; \\ 0, & f = 0; \\ i, & f < 0. \end{cases}$$

525 Then

$$F[\tilde{x}(t)] = \tilde{X}(f) = F\left[\frac{1}{\pi t} * x(t)\right] = F[x(t)] \cdot F\left(\frac{1}{\pi t}\right) = -i[\text{sign}(f)] \cdot X(f).$$

526 Multiplying both parts of the last expression by  $i[\text{sign}(f)]$ , we get

$$i[\text{sign}(f)] \cdot \tilde{X}(f) = X(f).$$

527 This equation is used for the numerical solution of the Hilbert transform pair. The algorithm of calculating

528 the Hilbert transform consists of three steps:

529 1) to calculate the spectrum  $X(f)$ :

$$X(f) = F[x(t)];$$

530 2) to apply the expression  $i[\text{sign}(f)] \cdot \tilde{X}(f) = X(f)$  for calculating  $\tilde{X}(f)$ :

$$\tilde{X}(f) = -i[\text{sign}(f)] \cdot X(f)$$

531 3) to calculate  $\tilde{x}(t)$ :

532 
$$\tilde{x}(t) = F^{-1}[\tilde{X}(f)].$$

533 These three steps are used in Matlab for the calculation of Eqs.B2 via the function *Hilbert*.

534 More details about numerical solution of the Kramers-Kronig transforms based on the FFT algorithm are  
535 presented in P.Bruzzoni et<sup>19</sup>.

## 536 References

- 537 1. D. Wetzel and J. Reffner, *Cereal Foods World*, 1993, **38**, 9-20.  
538 2. B. Mohlenhoff, M. Romeo, M. Diem and B. R. Woody, *Biophys J*, 2005, **88**, 3635-3640.  
539 3. G. Mie, *Ann. Phys.(Leipzig)*, 1908, **25**, 377-452.  
540 4. H. C. Van De Hulst, *Light scattering by small particles*, Courier Corporation, 1957.  
541 5. P. Bassan, H. J. Byrne, F. Bonnier, J. Lee, P. Dumas and P. Gardner, *Analyst*, 2009, **134**, 1586-1593.  
542 6. P. Bassan, A. Kohler, H. Martens, J. Lee, H. J. Byrne, P. Dumas, E. Gazi, M. Brown, N. Clarke and P.  
543 Gardner, *Analyst*, 2010, **135**, 268-277.  
544 7. P. Bassan, A. Kohler, H. Martens, J. Lee, E. Jackson, N. Lockyer, P. Dumas, M. Brown, N. Clarke and  
545 P. Gardner, *Journal of Biophotonics*, 2010, **3**, 609-620.  
546 8. P. Bassan, A. Sachdeva, A. Kohler, C. Hughes, A. Henderson, J. Boyle, J. H. Shanks, M. Brown, N. W.  
547 Clarke and P. Gardner, *Analyst*, 2012, **137**, 1370-1377.  
548 9. A. Kohler, J. Sulé-Suso, G. D. Sockalingum, M. Tobin, F. Bahrami, Y. Yang, J. Pijanka, P. Dumas, M.  
549 Cotte, D. G. van Pittius, G. Parkes and H. Martens, *Appl Spectrosc*, 2008, **62**, 259-266.  
550 10. T. van Dijk, D. Mayerich, P. S. Carney and R. Bhargava, *Appl Spectrosc*, 2013, **67**, 546-552.  
551 11. R. Lukacs, R. Blümel, B. Zimmerman, M. Bağcıoğlu and A. Kohler, *Analyst*, 2015, **140**, 3273-3284.  
552 12. L. D. Landau, J. Bell, M. Kearsley, L. Pitaevskii, E. Lifshitz and J. Sykes, *Electrodynamics of continuous*  
553 *media*, Elsevier, 1984.  
554 13. J. L. Ilari, H. Martens and T. Isaksson, *Appl Spectrosc*, 1988, **42**, 722-728.  
555 14. H. Martens and E. Stark, *Journal of Pharmaceutical and Biomedical Analysis*, 1991, **9**, 625-635.  
556 15. A. Kohler, C. Kirschner, A. Oust and H. Martens, *Appl Spectrosc*, 2005, **59**, 707-716.  
557 16. N. K. Afseth and A. Kohler, *Chemometrics and Intelligent Laboratory Systems*, 2012, **117**, 92-99.  
558 17. B. Zimmermann and A. Kohler, *Appl Spectrosc*, 2013, **67**, 892-902.  
559 18. R. P. Kanwal, *Linear integral equations*, Springer Science & Business Media, 2013.  
560 19. P. Bruzzoni, R. Carranza, J. C. Lacoste and E. Crespo, *Electrochimica acta*, 2002, **48**, 341-347.

561

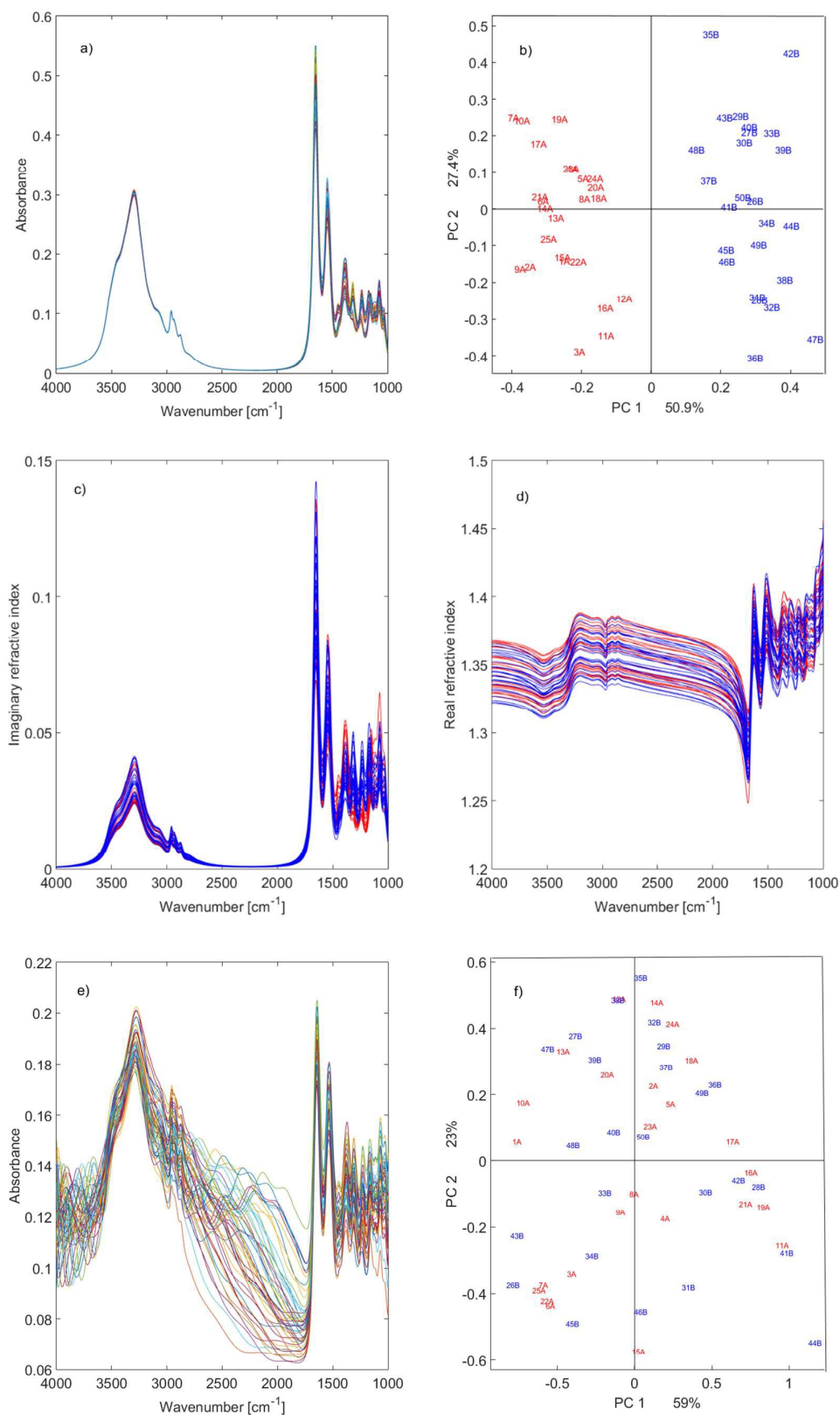


**Figure 1.** (a) A set of simulated pure absorbance spectra. (b) PCA of simulated pure absorbance spectra. (c) Imaginary part of the refractive index obtained from the simulated absorbance spectra (d) Real part of the refractive index obtained from the simulated absorbance spectra. (e) Apparent absorbance spectra obtained by employing exact Mie theory taking into account the optical setup of an infrared microscope. (f) PCA of simulated apparent absorbance spectra.

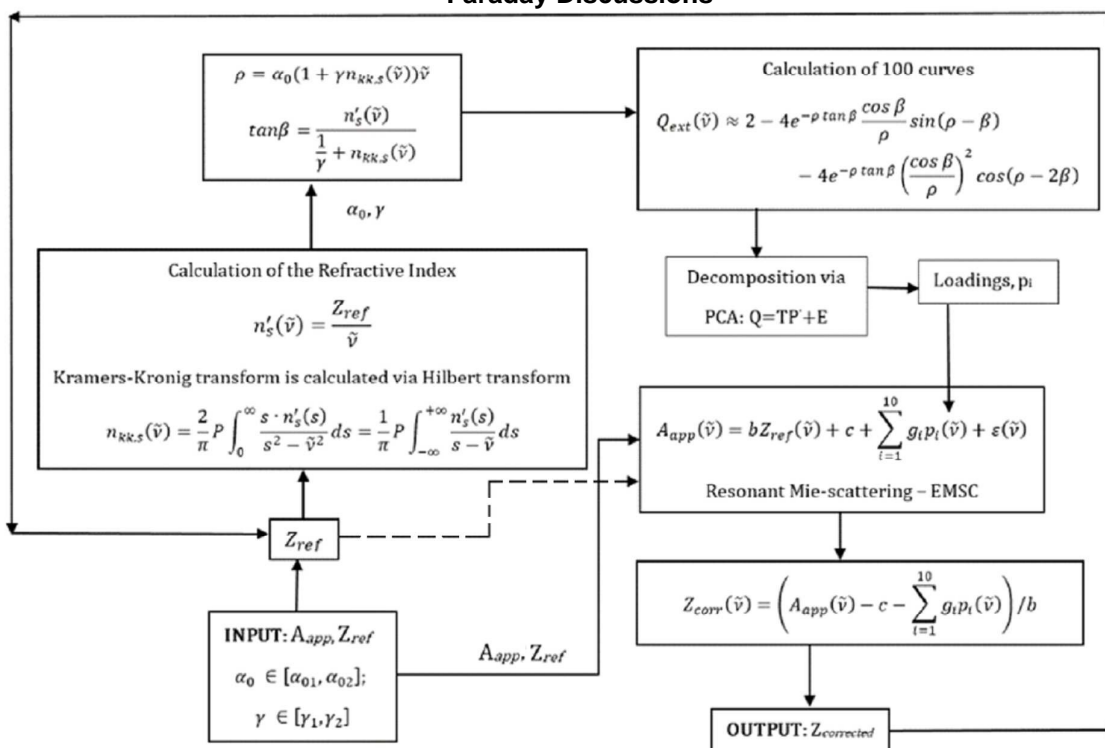


**Figure 2:** Schematic illustration of the iterative algorithm for the retrieval of the pure absorbance spectrum from the apparent absorbance spectrum. After each iteration, a new estimate of the pure absorbance spectrum is obtained. The next iteration is initialized by using the estimate of the pure absorbance spectrum for updating the real and imaginary parts of refractive index for the iterative algorithm.

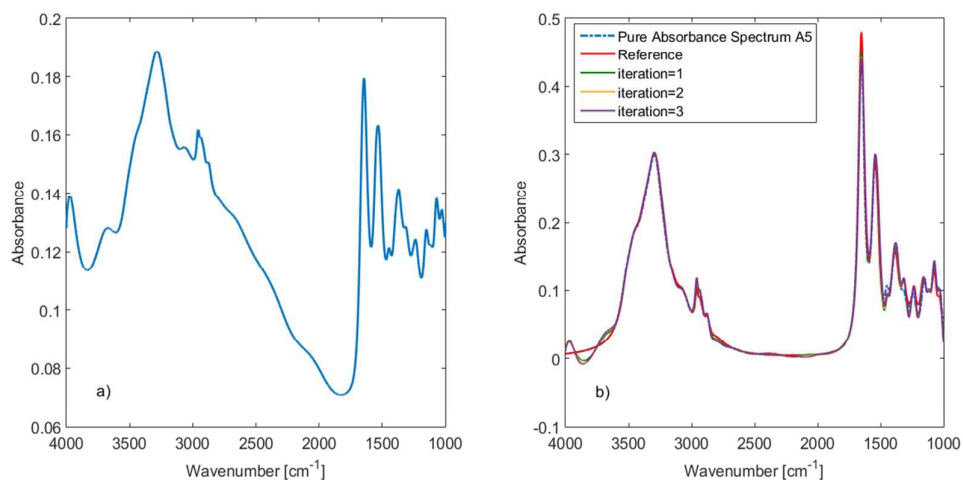


**Figure 3.** (a) An example of a simulated apparent absorbance spectrum is shown. (b) Spectra corrected by an iterative EMSC meta-model employing the Van De Hulst approximate formula with complex refractive index are shown. Corrected spectra for iteration 1, 2 and 3 of the correction algorithm (green, brown and violet, respectively) are close to the underlying pure absorbance spectrum (blue dashed line) and different from the reference spectrum (red line) employed. For simulation of the apparent absorbance spectrum in (a) we used the parameters  $n_0 = 1.35$  and  $a = 3.81 \mu m$ .

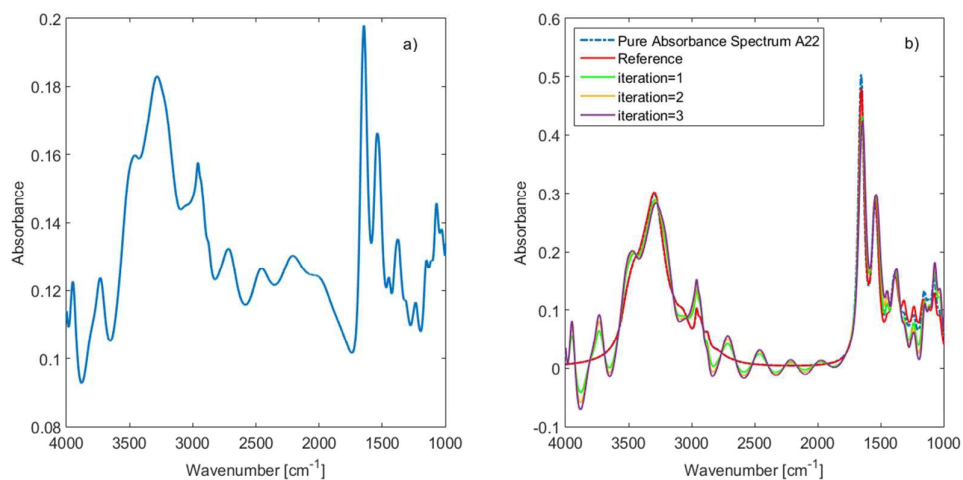


**Figure 4.** (a) Apparent absorbance spectrum containing ripples. For the simulation of the apparent absorbance spectrum the parameters  $n_0 = 1.36$  and  $a = 5.12 \mu\text{m}$  were used. (b) The corrected spectra for iteration 1, 2 and 3 of the correction algorithm (green, brown and violet, respectively). They still contain the ripple structure. As expected, the EMSC meta-model employing the Van De Hulst approximate formula with complex refractive index does not correct the ripples.

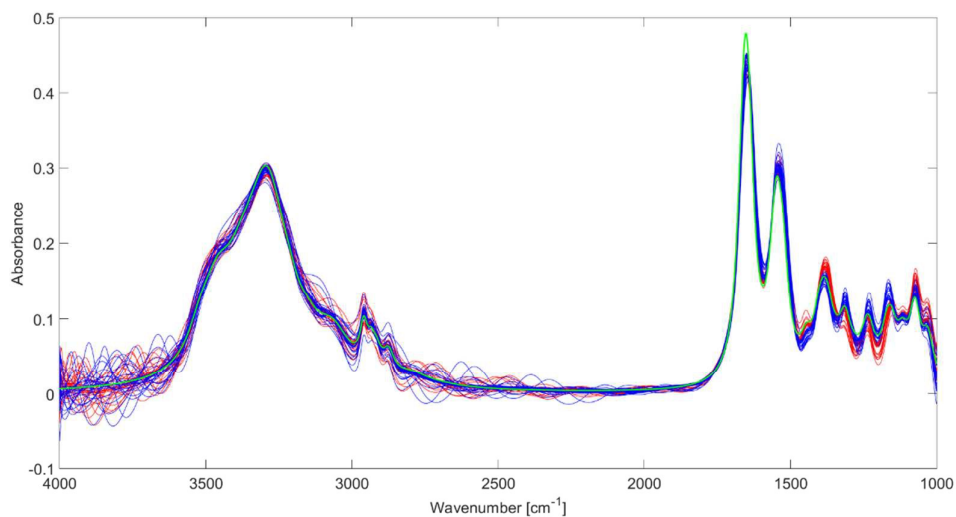


**Figure 5.** The complete set of simulated apparent absorbance spectra shown in Fig.1c is corrected by the algorithm presented in this paper. The spectra that correspond to red scores of pure absorbance spectra in Fig 1b are drawn in red; the spectra that correspond to blue scores of pure absorbance spectra in Fig. 1b are marked blue. The reference spectrum is shown in green. Some corrected absorbance spectra contain ripples. As expected, the EMSC meta-model employing the Van de Hulst formula with complex refractive index does not remove ripples.

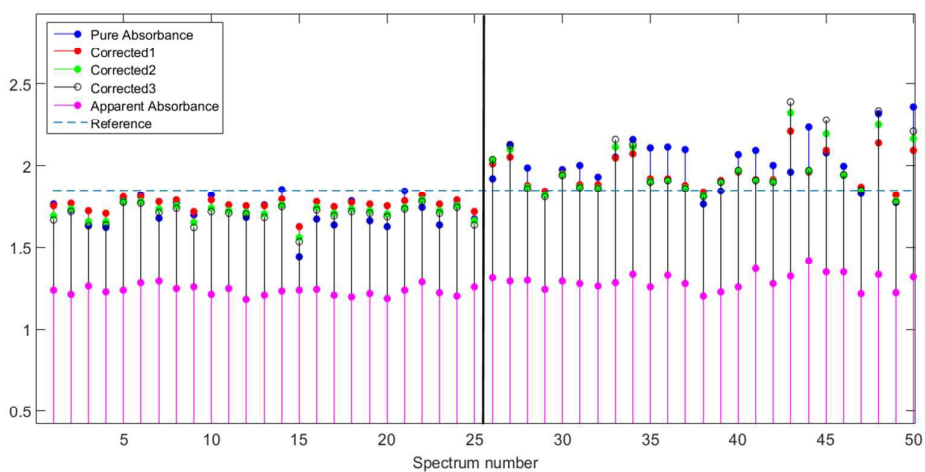


**Figure 6:** The peak ratio is shown for the bands at  $1546\text{ cm}^{-1}$  and  $1387\text{ cm}^{-1}$  for the simulated pure absorbance spectra (blue), for iteration 1, 2 and 3 of the correction algorithm (red, green and black, respectively) and for the apparent absorbance (magenta). The ratio for the reference spectra is plotted as the blue dashed line for comparison.

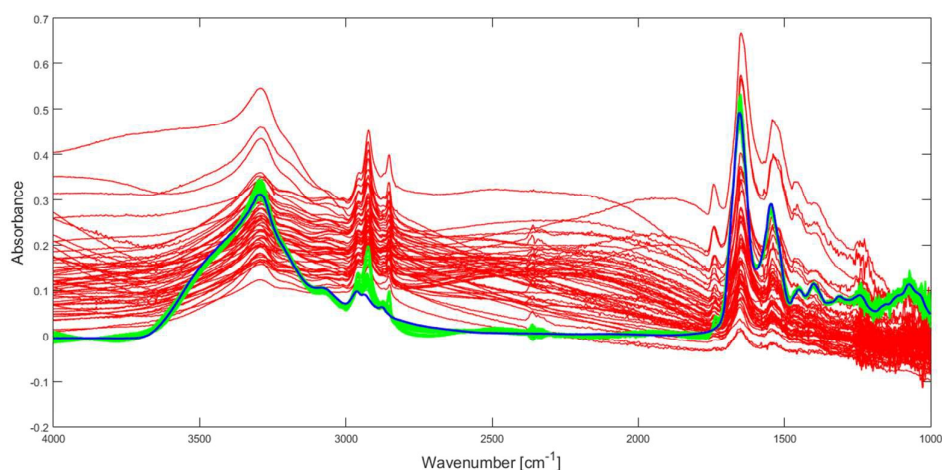


**Figure 7.** The measured infrared microspectroscopy spectra of lung cancer cells are shown in red together with the corrected spectra in green. For the correction one iteration step was used. As a reference spectrum (in blue) the matrigel spectrum was used.

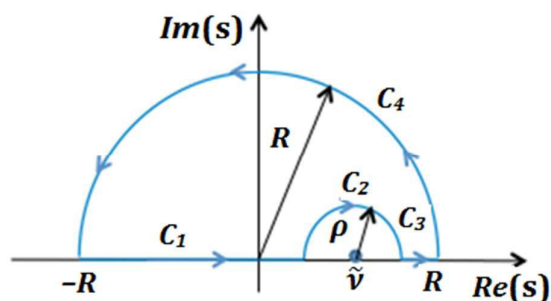


**Figure 8.** Contour in the complex plane used to derive the Kramers-Kronig relations. The integration path, which is skirting the singularity point  $s = \tilde{\nu}$ , is indicated by arrows. The radius  $R$  of the outer semicircle tends to infinity. The radius  $\rho$  of the small semicircle about  $\tilde{\nu}$  tends to zero.